International Journal of Impact Engineering, Volume 30, Issue 7,
Fifth International Symposium on Impact Engineering, August 2004,Pages 853-872

FAILURE PREDICTION FOR ADVANCED CRASHWORTHINESS OF TRANSPORTATION VEHICLES

Anthony Pickett* (Cranfield University, UK)

Thomas Pyttel, Fabrice Payen (ESI GmbH, Eschborn, Germany)

Franck Lauro (University Valenciennes, France)

Nikica Petrinic (University Oxford, UK)

Heinz Werner (BMW AG, München, Germany)

Jens Christlein (AUDI AG, Neckarsulm, Germany)

* Author for correspondence: Cranfield University, SIMS, Bedfordshire, MK43 OAL.

During the past two decades explicit Finite Element crashworthiness codes have become an indispensable tool for the design of crash and passenger safety systems. These codes have proven remarkably reliable for the prediction of ductile metal structures that deform plastically; however, they are not reliable for joining systems and materials such as high strength steels, plastics and low ductility lightweight materials all of which are liable to fracture during the crash event.

In order to improve crash failure prediction of materials and joining systems the CEC has recently funded a three year European research project dedicated to this topic. Specifically the project concerned Aluminium, Magnesium, High Strength Steels, Plastics and two primary joining techniques; namely spotwelds and weldlines. Numerous new developments were undertaken including improved failure laws,

adaptive meshing and element splitting to treat crack propagation. In the case of sheet stamping, investigations have also tried to account for process history effects and the metallurgical changes that occur during manufacture. This project has recently finished and this paper presents some of the key research results of the work concerning materials failure modelling.

Keywords: Crashworthiness, Material modelling, Failure modelling, Simulation.

1 Introduction

Traditionally automotive ‘body in white’ structures are manufactured using individual stamped parts that are spotwelded together. The predominant material used is low cost ductile sheet metal which can be readily stamped to shape and joined. During the past 20 years crashworthiness simulation of these structures has proven remarkably good, largely because crashworthiness explicit Finite Element (FE) codes, such as [1, 2] can accurately predict the simple plastic bending and stretching deformation mechanisms that occur. It is not usually necessary to predict material failure.

In recent years automotive manufacturers are increasingly using new lightweight materials to reduce weight; these include Plastics, Composites, Aluminium, Magnesium and new types of High Strength Steels. Many of these materials have limited strength or ductility, or may be used in highly loaded applications; in each case rupture is a serious possibility during the crash event. Furthermore, the joining of these materials presents another source of potential failure. Both material and joining failure will have serious consequences on vehicle

crashworthiness and must be predictable if the numerical model is to be reliably used in the design process.

A large amount of research work concerning numerical modelling of material failure can be found in the literature [3]. However, unfortunately, this work is usually not appropriate for practical crashworthiness analysis using an explicit Finite Element code which is the established numerical technique for crash simulation. Consequently, it has been necessary to undertake a dedicated European (Framework V) research project, IMPACT [4], to develop models and methodologies for failure prediction. This work has been carried out within the commercial crashworthiness FE code PAM-CRASH [1].

The IMPACT project was initiated in 2000 and completed in 2003. New (and existing) material failure laws for both thermo visco-elastic plastics and advanced metals were investigated with special emphasis to accurately predict both initial material failure and subsequent crack propagation. Crack propagation should be accurately represented in order to evaluate its effect on the structure integrity and crashworthiness; for this two techniques using adaptive meshing and element splitting have been studied. The work also accounted for changes in material morphology that result from the manufacturing process; this will influence failure limits for metal stamped parts due to the shaping operation.

2 Constitutive modelling of failure and solution strategies

Two different approaches are considered for material failure modelling. First, a micro-mechanical approach using solid Finite Elements is used to provide a

reasonably accurate prediction of the 3D stress distribution in the necking failure location and around a propagating crack. If suitably fine meshing and appropriate material laws are selected then both failure initiation and crack propagation can be represented; clearly this approach leads to large FE models and is therefore restricted to component failure analysis. The second approach is more practical for large scale crash analysis and uses conventional shell elements and macro-mechanical failure criteria to identify the onset of material failure. This law cannot treat crack propagation and consequently element splitting and energy based criteria are applied for this phase of failure. The following sections briefly outline both approaches.

2.1 Micro-mechanical models

The term ‘micro- mechanical models’ is used here to classify a modelling approach using detailed 3D solid elements which attempt to represent local necking, the formation of a crack and crack propagation. During the course of the project phenomenological constitutive models with failure criteria based upon micro-mechanical void growth using the Gurson model [5] and the Gologanu model [6] were developed, together with the Lemaitre mezzo-scale damage mechanics model [7] and the Wilkins failure criteria [8]; each of these models is briefly described below.

2.1.1 The Gurson damage model

In recent years the Gurson constitutive model [5] has been widely used to treat progressive microrupture of ductile metals. This model represents the commonly observed stages of ductile fracture, which include:

1) The formation of voids around inclusions and second phase particles.
2) The growth of voids due to plastic straining and hydrostatic stress.
3) The coalescence of growing voids leading to fracture.

These mechanisms are represented by introducing strain softening to the von Mises elasto-plastic yield surface to treat damage growth. The nucleation rate of micro-voids is expressed as a Gaussian distribution over plastic strains. The mean effective plastic strain ε_N, the nucleated microvoid volume fraction f_N and standard deviation of this Gaussian distribution S_N are three Gurson parameters that must be found. The growth is controlled by plastic strain and the hydrostatic state of stress. Additional parameters must be given for initial void content f_0, the critical microvoid volume fraction at the onset of coalescence f_C and the critical fraction of voids at which fracture occurs f_F. Usually 'inverse engineering' techniques are used to determine the Gurson parameters by correlating test and analysis results for failure load and cross section dimension changes which occur at the neck of a tensile coupon test.

The Gurson model is a quadratic formulation of plastic potential which can also be used as a yield function in which σ_{eq} is the macroscopic equivalent stress, σ_M is the elasto-viscoplastic flow stress, σ_m is the mean stress (= $(\sigma_{11} + \sigma_{22} + \sigma_{33}) / 3$), q_1

and q_2 are two material constants and f^* is the Tvergaard and Needleman effective void volume fraction [9],

$$\phi_{evp} = \frac{\sigma_{eq}^2}{\sigma_M^2} - \varphi = 0 \ ,$$

where $\varphi = 1 + (q_1 f^*)^2 - 2q_1 f^* \cosh(\nu) \ , \quad \nu = \frac{3}{2} q_2 \frac{\sigma_m}{\sigma_M}$.

The microvoids volume fraction rate is expressed by,

$$\dot{f} = \dot{f}_{growth} + \dot{f}_{nucleation} \ .$$

where the growth of existing voids is given by,

$$\dot{f}_{growth} = (1 - f)\dot{\varepsilon}_{kk} \ .$$

and the void nucleation is controlled by the plastic strain and takes the form,

$$\dot{f}_{nucleation} = \frac{f_N}{S_N \sqrt{2\pi}} exp\left\{ -\frac{1}{2}\left(\frac{\varepsilon_M - \varepsilon_N}{S_N} \right)^2 \right\} \dot{\varepsilon}_M \ .$$

The effective void volume fraction f^* is then defined by,

$$f^* \begin{cases} f & for \quad f \le f_c \\ \dfrac{1}{q_1} - f_c & \\ f_c + \dfrac{q_1}{f_F - f_c}(f - f_c) & for \quad f > f_c \end{cases}$$

where f_c and f_F are two additional, previously defined, fitting parameters.

The main disadvantages of the model are determination of the Gurson parameters and, more importantly, that damage is only a consequence of hydrostatic loading. Damage and failure due to shear loading is not considered. Furthermore,

studies in the IMPACT project on tensile loaded notched specimens have found that the optimal Gurson parameters vary with notch diameter; this would indicate that the Gurson parameters are not a constant, but may be a function of the state of triaxial loading.

2.1.2 The Gologanu damage model

The Gologanu model extends the Gurson model by taking into account the changes in microvoid shape that occur during deformation. Indeed, the Gologanu model considers cavities of ellipsoidal form, whose shape and orientation can evolve. The plastic potential is a quadratic formulation which can also be used as a yield function in which σ_{eq} is the macroscopic equivalent stress, σ_M is the elasto-viscoplastic flow stress, q_1, α_1 and α_2 are material parameters introduced in order to converge the model with full numerical analyses of periodic arrays of voids; f^* is the Tvergaard and Needleman's coalescence function,

$$\phi_{evp} = C\frac{\left\|\sigma' + \eta\sigma_H X\right\|}{\sigma_M^2} - \varphi = 0 \quad ,$$

where $\varphi = 1 + \left(q_1 f^*\right)^2 - 2q_1 f^* \cosh(\nu), \quad \nu = \frac{\kappa\sigma_H}{\sigma_M}, \quad \sigma_H = (1-2\alpha_2)\sigma_{11} + \alpha_1\sigma_{22}$.

The parameters κ, η, C and X depend on the geometry of the ellipsoid void, σ_H is the mean stress and the von Mises norm is given by,

$$\left\|\sigma_{ij}\right\| = \sqrt{\frac{3}{2}\sigma_{ij}\sigma_{ij}} \quad .$$

Numerically, in pure shear loading, there is no damage evolution and consequently no rupture. In order to consider damage due to shearing the damage evolution law is modified to comprise of the sum of the classical law and a new part due to shear loading giving,

$$\dot{f} = \dot{f}_{growth} + \dot{f}_{nucleation} + \dot{f}_{shear}$$

In pure shear it is commonly accepted that the voids experience a rotation without any change in growth and it appears that nucleation can be generated. Consequently, the damage evolution law due to shearing takes the form of a statistical law, similar to the nucleation evolution law, but taking into consideration the shearing strain and the shearing strain rate. It is defined by,

$$\dot{f}_{shear} = \frac{f_S}{S_S\sqrt{2\pi}} \; exp\left(-\frac{1}{2}\left(\frac{\varepsilon_{xy} - \varepsilon_S}{S_S} \right)^2 \dot{\varepsilon}_{xy} \right).$$

The identification of the damage parameters controlled by the shearing strains is carried out by the inverse method using an Arcan type test [10]. Figure 1 shows the tensile simulation of a non-axisymmetric double V-notched specimen; a) shows the initial finite element modelling; b) and c) are the damage distribution at the end of the process using the Gurson and Gologanu models respectively. Figure 1d gives the orientation and shape evolution S at the end of the rupture process for an initial prolate void shape using the Gologanu model. From this Figure it can be seen that including changes in the void shape does allow anisotropic damage to be represented and more correctly captures the failure process. It should be noted, however, that the implementation here was only for shell element which limits accuracy since triaxial stresses, particularly in the necking zone, are neglected. A

solid element would lead to better results but would be CPU time consuming; a further improvement could be to use an energy criterion to dissipate energy as each failed element is eliminated.

2.1.3 The Lemaitre damage model

The framework of continuum damage mechanics is used to describe the development of damage under mechanical loadings, its progression up to the initiation of a macro-crack and finally the growth of this macro-crack during failure of the component. The original model for ductile fracture was established for isotropic damage conditions and later extended to include anisotropic damage development [11,12]. The basic ingredient of the model is the damage law used either in monotonic loadings for ductile fracture, or in cyclic loadings for low cycle or high cycle loadings. This damage law depends on the damage variable D and the strain energy density release rate which is the principal variable governing the phenomenon of damage and is expressed by,

$$Y = \frac{W_e}{1-D}.$$

The strain energy rate W_e is split into its shear and hydrostatic parts, and leads to the following expression,

$$W_e = \frac{(1+\nu)}{2E(1-D)}\langle\sigma_{ij}\rangle\langle\sigma_{ij}\rangle - \frac{\nu}{2E(1-D)}\langle\sigma_{ij}\rangle^2.$$

in which $\langle\sigma_{ij}\rangle = \sigma_{ij}$ if $\sigma_{ij} \geq 0$ and $\langle\sigma_{ij}\rangle = 0$ if $\sigma_{ij} < 0$. Finally, the damage evolution during plastic straining is defined by the following expression,

$$\dot{D} = \left(\frac{Y}{S}\right)^{S} \dot{\boldsymbol{\varepsilon}}^{p} \quad if \quad \boldsymbol{\varepsilon}^{p} > \boldsymbol{\varepsilon}_{D} \ ,$$

in which *S* and *s* are material coefficients, ε^p is the effective plastic strain and ε_D is the plastic strain at damage threshold.

As the damage evolution is localised in the large plastic strain zone the evolution damage law and the threshold parameters must be identified in consequence. A direct identification approach or local approach is used essentially on uniaxial monotonic and cyclic tests, Figure 2. For a better identification experiments in the largest possible domains of stresses, strains, time and number of cycles are needed [7]. An identification approach using inverse techniques is used to find the damage parameters by correlating experimental and numerical macroscopic measurement strongly dependent on the parameters [13,14]. Tensile tests on thin notched specimens are used as mechanical tests to measure macroscopic responses and variations of inner radius and force with respect to elongation of the specimen are used to correlate test and numerical models.

In order to better represent the behaviour of an aluminium alloy, an anisotropic potential can be used [15,16,17]; for the present case, a Hill 48 potential is considered. The above damage model for anisotropic materials has been implemented in 2D shell and 3D solid elements. The damage parameters were identified as discussed above and applied to a validation example consisting of the three points bending of an aluminium extruded section with an initial slit (starter crack) on the lower face to localise failure initiation, Figure 3. This test was carried

out dynamically and the numerical and experimental results are found to be in good agreement in terms of failure path and energy level, Figure 4.

2.1.4 The Wilkins failure criteria

An early continuum model for void nucleation is due to Argon, Reference [18]. This model proposes that the decohesion stress σ_c is a critical combination of the hydrostatic σ_m and the effective von Mises stress σ_e,

$$\sigma_c = \sigma_m + \sigma_e \ .$$

In a similar approach Wilkins [8] proposed a failure criterion based of the summation of the increment of plasticity, in this case two weighting functions, w_1 and w_2, are introduced to independently weight damage due to the hydrostatic and deviatoric loading components. This law then defines cumulative damage (D) to be given by,

$$D = \int w_1 w_2 \, d\bar{\varepsilon}_p$$

where, $d\bar{\varepsilon}_p$ is the equivalent plastic strain,

w_1 is the hydrostatic-pressure weighting term = $\left(\frac{1}{1+aP}\right)^{\alpha}$,

w_2 is the deviatoric weighting term = $(2-A)^{\beta}$,

A = $Max\left(\frac{s_2}{s_3}, \frac{s_2}{s_1}\right)$, $\quad s_1 \geq s_2 \geq s_3$.

The hydrostatic stress is denoted P, and s_1, s_2 and s_3 are the principle stress deviators; the material constants a, $\propto$ and β are found from experimental testing which should, ideally, cover a wide range of loading conditions ranging from pure hydrostatic to pure shear. Again, Finite Element solutions and 'inverse engineering' techniques are used to correlate test and simulation results and determine 'best fit' values for the failure constants.

Within this work tensile parallel sided specimens and notched specimens (8mm, 4mm and 0.25mm diameter) are used to determine the model failure parameters. As a validation exercise the previous extruded aluminium example under three point bending was studied. In this case a mesh of shell elements was used for most of the section with only 3D solids being used around the area of failure, Figure 5, in order to reduce CPU time. Figure 5 shows the comparison between experiment and simulation for impact force time histories and direction of crack propagation. In general the results are encouraging and a good agreement is found; in this case the difference between the Hill 48 and standard von Mises plasticity are not significant.

An industrial application of the Wilkins failure model is shown in Figure 6, which considers the dynamic loading of an Aluminium space frame structure. The mode of loading is side impact using a 179mm diameter rigid post. The modelling used a hybrid approach in which most of the structure used simple shell elements which were locally refined in critical areas with detailed 3D solid element meshes at which the failure criteria was applied. The failure parameters for the Wilkins model were obtained from tensile tests on notched specimens. Whilst this modelling approach is costly in terms of preparation and CPU time it does provide predictive results and all of the main failure locations were correctly identified. Future work will

consider the automated methods introduced in section 3.2 which will have the potential to identify all possible failure locations and restrict mesh refinement only to these zones.

2.1.5 Comparison of the Micro- failure models

The Gurson model can realistically represent failure provided the loading state used to determine the Gurson parameters is similar to the state of loading in the rupture zone of the structure and is predominantly hydrostatic. Improvements are possible using the Gologanu model to take into account anisotropic damage; however, this model introduces several additional parameters that are not easily identified. The Lemaitre model appears to give encouraging results and uses a well defined, if somewhat laborious cyclic testing procedure, to determine the model damage parameters. Finally, the Wilkins failure model is easily understood and relatively straightforward to calibrate against appropriate test coupons; consequently, it has been well received by industrial partners in the IMPACT project.

2.2 Macro-mechanical models

Modern crash simulation models typically use element edge lengths of 5 to 15 mm. The previous micro- mechanical failure laws are unsuitable for such meshes and alternative methods must be sought. In the IMPACT project two different approaches were developed and tested:

1. Failure prediction based on the onset of local instability.
2. Failure based on fracture curves.

The first approach has been applied to sheet metal components made of high strength TRIP, complex phase and dual phase steels, whereas the second was used for automotive plastics. Both are briefly described below.

2.2.1 Stability criteria for fracture

For sheet metal the onset of instability can be used as a fracture criterion. This loss of stability is analysed by considering biaxial tension on a rectangular element of the sheet. Usually instability manifests itself by local thinning (necking) in a groove running perpendicular to the larger principal stress; an analytical solution to this stability problem is provided by Marciniak [19], Figure 7a. At the onset of instability the local strains associated with this groove equal the global strains and can therefore be used as a measure of failure strains in a shell element, Figure 7b. After instability large local strains localize in the neck leading to a large difference between local and global strains, Figure 7c.

In the IMPACT project the CRACH algorithm [20] is used to determine instability limits; this incorporates the following improvements to the original Marciniak model:

- A refined model of the geometry of the localized neck area is used.
- A refined material model with anisotropic hardening including the ‘Bauschinger’ effect.
- Inclusion of parameters to account for process history effects such as solution heat treatment and age hardening.

In practice the part to be considered for crash failure analysis must first be simulated as a metal stamping problem. Information on the complete deformation history for each element is needed and stored during stamping; this is then mapped to the new crash mesh prior to the crash simulation. During the crash simulation information on critical elements is exchanged between the crash simulation model and the CRACH algorithm to provide a continuous update on the stability limits for the elements. If a state of instability is reached the element is eliminated.

The CRACH algorithm requires an extensive test program to characterise the dynamic failure of pre-strained material. Specimens were prepared with different pre-strain conditions and then tested dynamically to failure. Most of this high strain rate testing work used a conventional Hopkinson bar; however, for the case of bi-axial loading a new dynamic multi-axial ‘bulge’ rig has been developed that allows such deformation to be applied to high strength thin-sheet specimens at elevated strain rates (>100/s), Figure 8. Also shown in Figure 8 is an example of the failure of a 100 mm diameter TRIP steel specimen.

The side impact study, Figure 9, illustrates the principle of this approach. The side structure analysed and the loading setup for the experiment and simulation model are shown in Figures 9a and 9b. The simulation is performed with a detailed shell element model having an average edge length of about 5 mm. The prediction of failure is based on the onset of instability as predicted by the CRACH algorithm. Figure 9c shows the test location of failure in the B pillar which is also observed in the numerical analysis.

2.2.2 Constitutive and failure model for plastics

Typical polymers used in automotive applications are ductile thermoplastics which are used for a wide variety of applications including interior trim. These applications must meet certain energy absorption requirements to minimise occupant injury. For this work two commercial plastics were investigated:

1. **HIFAX CR 1171 G 2116 from Basell Polyolefins:** This is a semicristalline 'filled' Polypropylene (PP) copolymer.
2. **BAYBLEND T65 792 from Bayer:** This is an amorphous 'unfilled' Polycarbonate/Acrylonitrile-Butadiene-Styrene (PC-ABS) blend.

Clearly the mechanical behaviour of metals and plastics are very different; never-the-less, it has been proposed that the elasto-plastic von Mises law is a reasonable basis to describe the non linear response of plastics, Reference [3]. The main difficulty is to provide a hardening law that can correctly describe the rate and temperature dependent behaviour of these materials. An example stress-strain response for HIFAX (Polypropylene) is shown in Figure 10. A simple law that reasonably characterises the form of the stress-strain curve for most plastics is the G'Sell model [21], with four curve fitting parameters,

$$\boldsymbol{\sigma} = k\left[1 - exp^{(-w\boldsymbol{\varepsilon})}\right] exp^{(h\boldsymbol{\varepsilon}^2)} \left(\boldsymbol{\varepsilon}^{\bullet} / \boldsymbol{\varepsilon}_0^{\bullet}\right)^m ,$$

where σ and ε are the effective stress and strain, *k* is a scaling factor, $\left[1 - exp^{(-w\boldsymbol{\varepsilon})}\right]$ is a visco-elastic term to describe the beginning of the stress-strain curve and $e^{h\varepsilon^2}$ controls strain hardening at large strains. Finally, $\left(\varepsilon^{\bullet} / \varepsilon_0^{\bullet}\right)^m$ expresses the strain rate sensitivity as a power law. The material constants *k, w, h* and *m* are determined

for different temperatures and linear interpolation is used for any other temperature state. G'Sell parameters for HIFAX and BAYBLEND were determined from experimental testing and are given in Table 2. Strain rate effects are included by determining these factors for different rates of loading and using linear interpolation for other strain rates.

The high sensitivity of these materials to thermal changes suggests that temperature increase due to internal material deformation should also be included. The adiabatic increase in temperature can be expressed by the simple relation,

$$\Delta T = c * Q * \Delta \boldsymbol{\varepsilon}_P ,$$

where ΔT is the temperature increment resulting from a plastic strain increment $\Delta \varepsilon_p$ for a material with heat capacity Q; c is a conversion constant usually assumed to be 0.9.

Experimental testing has also shown that failure in plastics is highly dependent on rate of loading and temperature. Consequently, a simple temperature and rate dependent failure criteria based on maximum principle strain has been used. The required information is defined via a set of curves, Figure 11a, from which failure for any strain rate and temperature condition may be interpolated. Figure 11b shows the application of the plastic constitutive law, with failure, for a constant rate and different temperature conditions. The abrupt point of failure is clearly seen in these curves.

An example application of this model is the impact of a thermoplastic (BAYBLEND) honeycomb plate, Figure 12, which is used for energy absorption in the A-pillars of a vehicle. The honeycomb plate was impacted with a sphere at different temperatures and with different velocities. Test and simulation results for the ductile

impact case at 85°C and the brittle impact case -35°C are shown in Figure 13. The constitutive model and simple macro- failure criteria give a good prediction of the changes in failure modes for both high and low temperature impact cases. The impact force time histories are also in good agreement with test results.

3 Numerical techniques

Two special developments to facilitate application of the material models have been made. First, techniques to automatically convert single shell elements to a patch of fine solid elements have been developed. This provides an automated procedure to locally apply micro- mechanical material models and limit CPU costs. In the case of macro- material modelling techniques have been developed to treat crack growth by splitting elements and allowing crack propagation dependent on energy based criteria. Both techniques are briefly illustrated.

3.1 Remeshing: Shells to solids

Generally shell elements having an edge legth of 5-15mm are appropriate for crash simulation. As mentioned previosly these elements are not suitable for micro-mechanical constitutive laws and detailed 3D solid elements must be used. The two element types can be combined to reduce CPU costs by using coarse shell elements with fine solid meshes only in areas of potential failure. Clearly a better approach is to automate this process and replace shell elements with solids elements only in areas that approach failure during the crash. Figure 14 shows the conversion of one shell element to a set of solids. For such a procedure the patch of solid elements of specific size must be generated and all constitutive variables, including damage

variables, must be mapped from the shells to the solid elements. Special constraints are also introduced to tie existing shell and solid elements to the new solids. Figure 14 shows the application of this technique to a simple example.

3.2 Shell element splitting

The macro-mechanical stability criterion presented in section 2.2.1 is only valid up to the point of fracture; thereafter the local stress distribution of a growing crack cannot be captured by the coarse shell model. This crack growth phenomenon can be approximately treated by splitting elements, Figure 15. The algorithm collects element information at nodal points and checks if the node belongs to a propagating crack and must be considered for opening. The direction of crack opening is assumed to be normal to the direction of maximum principal strain; fictitious forces control crack opening such that at full opening the Mode I fracture energy of the material over the area represented is absorbed.

4 Conclusion

The IMPACT project undertook an extensive program to test dynamically a range of automotive materials, develop constitutive models and validate the failure modelling of these materials on components. In total four different constitutive failure laws for metals have been studied and evaluated which are suitable for micro-mechanical analysis. Furthermore, a new macro-mechanical constitutive and failure law for rate and temperature dependent plastics and a macro-mechanical failure law based on instability fracture criteria for high strength steels have been developed and

validated. Other novel developments have included automatic mesh refinement and shell element splitting techniques to treat crack propagation. The work has been validated on several industrially relevant demonstrators where a good agreement between test and simulation results for failure prediction has been found.

Acknowledgements

The enthusiastic support of the IMPACT project partners VW, BMW, AUDI, IDIADA, ALCAN, ESI Group, CCP, Magna Steyr, CRF and the Universities of Oxford, Valenciennes and Cachan are gratefully appreciated. The partners would also like to thank the CEC for their financial support of this project under the Framework V programme.

References

1. PAM-CRASH, ESI Group, Rue Hamelin, BP 2008-16, 75761 Paris Cedex 16, France, http://www.esi-group.com.
2. DYNA3D, Livermore Software Technology Corporation, http://www.lstc.com.
3. T.L. Anderson, Fracture mechanics: Fundamentals and applications, 2nd Edition, CRC Press, 1995.
4. Framework V project, Improved failure prediction for advanced crashworthiness of transportation vehicles, 2000 – 2003, Project G3RD-CT-2000-00186.
5. A. L. Gurson, Continuum theory of ductile rupture by void nucleation and growth: Part I —Yield criteria and flow rules for porous ductile media, Engineering Material Technology, 99, pp 2-15 1977.
6. M. Gologanu, J.B. Leblond and J. Devaux, Approximate models for ductile metals containing non-spherical voids - Case of Axisymmetric prolate ellipsoidal cavities, Journal of the mechanics and physics of solids, 41, pp 1723-1754, 1993.
7. J. Lemaitre, A course of damage mechanics, Springer-Verlag, 1989.
8. M. Wilkins, Internal ESI documents and private communications.
9. V. Tvergaard and A. Needleman, Analysis of the cup-cone fracture in around tensile bar, Acta Metallurgica, Vol. 32, pp 157-169, 1984.
10. A. Michael, et al., Development and application of a crack tip opening displacement-based mixed mode fracture criterion, International Journal of Solids and Structures, Vol 37, 26, pp 3591-3618, June 2000.
11. A. Benallal, C. Comi and J. Lemaitre, Damage mechanics and localisation, In: Ju J.M. et al. (Eds), Vol. 13, 1992.
12. J. Lemaitre, R. Desmorat and M. Sauzay, Anisotropic damage law of evolution, Eur. J. Mech. A/Solids, 19, pp. 187-208, 2000.
13. F. Lauro, B. Bennani, P. Croix and J. Oudin, Identification of the damage parameters for anisotropic materials by inverse technique: application to an aluminium, Journal of Materials Processing Technology, 118, pp. 472-477, 2001.
14. P. Croix, F. Lauro and J. Oudin, Anisotropic damage for aluminium, International Journal of forming processes, 5, pp. 269-285, 2002.
15. R. Hill, A theory of the yielding and plastic flow of anisotropic metals. The hydrodynamics of non-Newtonian fluids, pp. 281-297, 1948.
16. F. Barlat and K. Lian, Plastic behaviour and stretchability of sheet metals. Part I: A yield function for orthotropic sheets under plane stress conditions, International Journal of Plasticity, 5, pp. 51-66, 1989.
17. F. Barlat, et al., Yield function development for aluminium alloy sheets, Journal of the mechanics and physics of solids, Vol. 45, pp. 1727-1763, 1997.
18. A.S. Argon, J. Im and R. Safoglu, Cavity formation from inclusions in ductile fracture, Metallurgical Transactions, Vol. 6A, pp. 825-837, 1975.
19. Z. Marciniak and K. Kuczinski, Limit strains in the processes of stretch forming sheet metal. Int. J. of Mechanical Sciences. Vol. 9, pp. 609 – 620, 1967.
20. H. Dell, et al., Continuous failure prediction model for nonlinear load paths in successive stamping and crash processes, SAE Paper 2001-01-1131, New sheet steel products and sheet metal stamping (SP-1614), SAE 2001 World Congress, Michigan, pp. 113-122, March 5-8, 2001.
21. P. Duffo, B. Monasse, J.M. Haudin, C. G'Sell and A. Dahoun, Journal of Materials and Science 30, 1995.

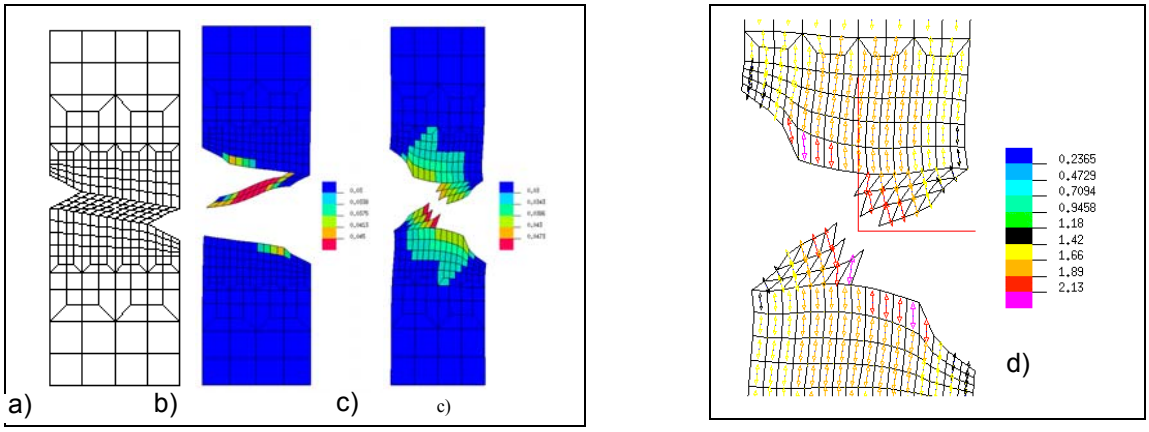

Fig 1: Comparison of rupture mechanisms for the Gurson and Gologanu models

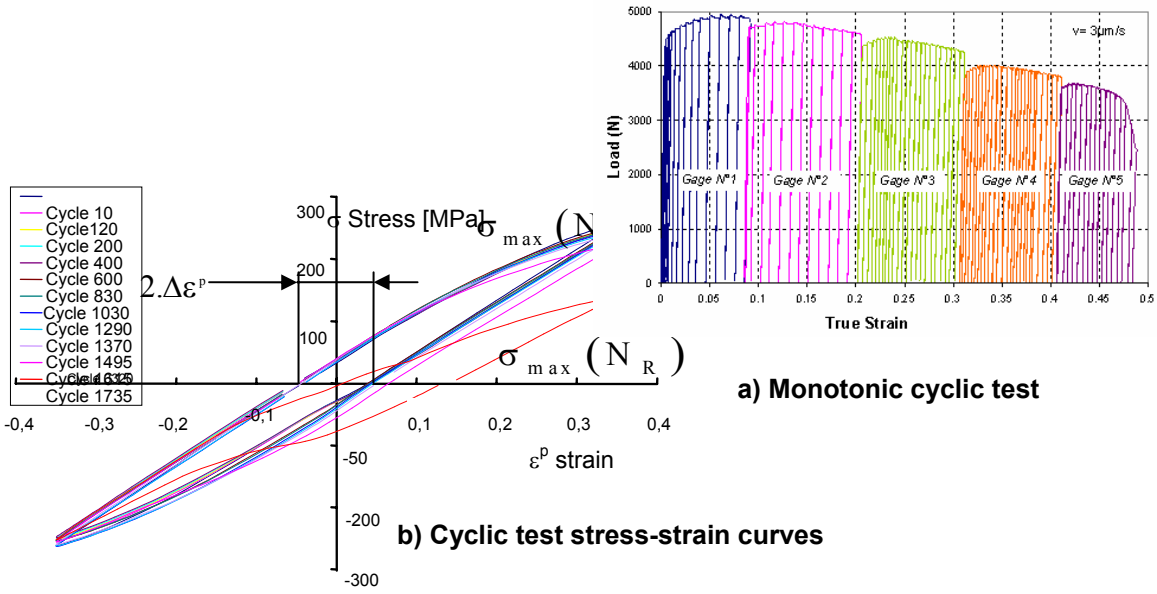

Fig 2: Monotonic cyclic test to determine the Lemaitre damage parameters

Gologanu's model	q_1	S_0	f_N	S_N	ε_N	f_c	f_F
	1.52	0.001	0.040	0.1	0.19	0.06	0.08
Lemaitre's model	ε_Δ	s	S	D_c			
	0.05	2	1.22	0.34			

Table 1: Damage parameters of 6014 T7 aluminium alloy.

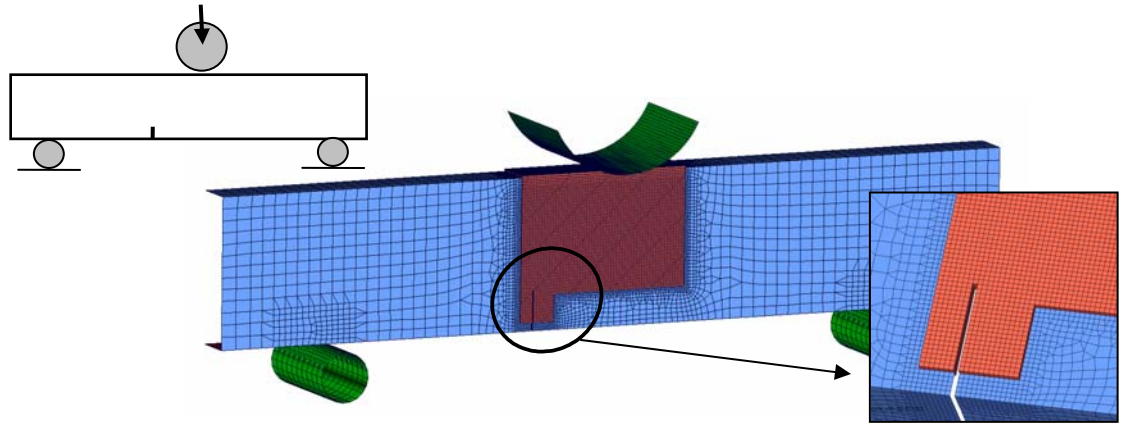

Fig 3: FE model for the 3 point bending of an aluminium section with 'starter crack'

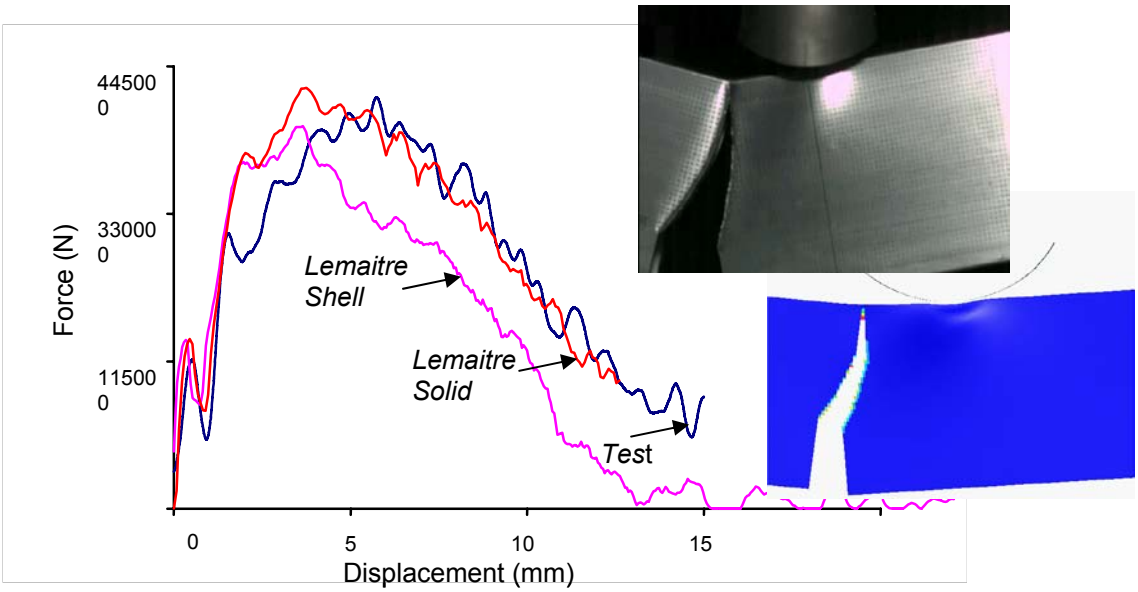

Fig 4: Experimental and simulation load versus displacement curves for shells and solids (Lemaitre model)

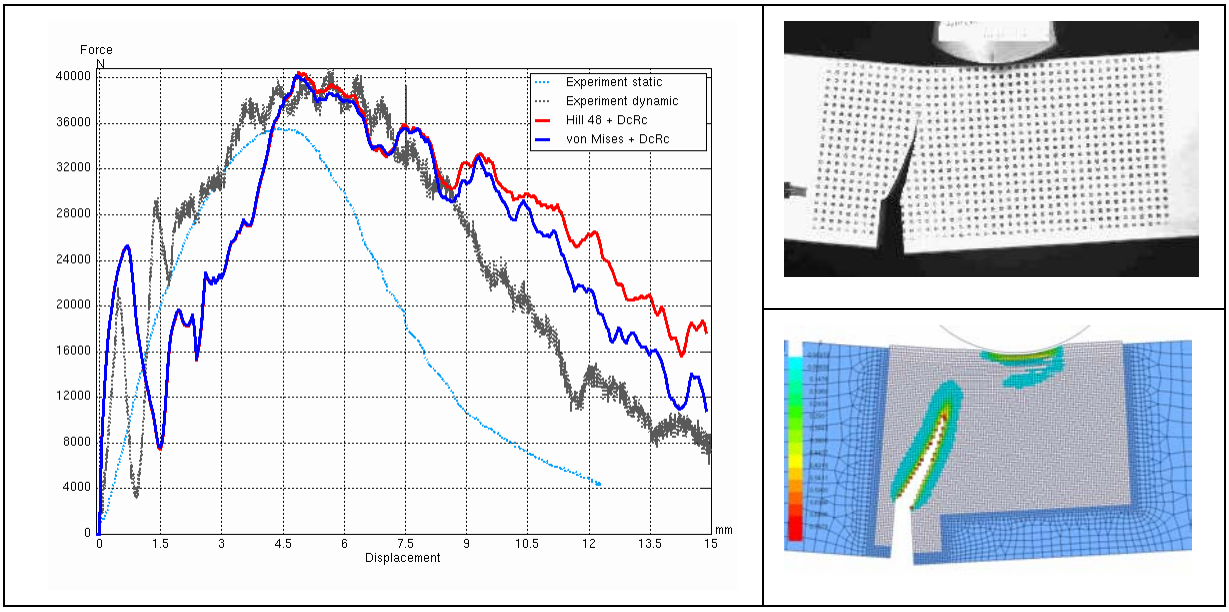

Fig 5: Experimental and numerical load versus displacement curves (Wilkins model)

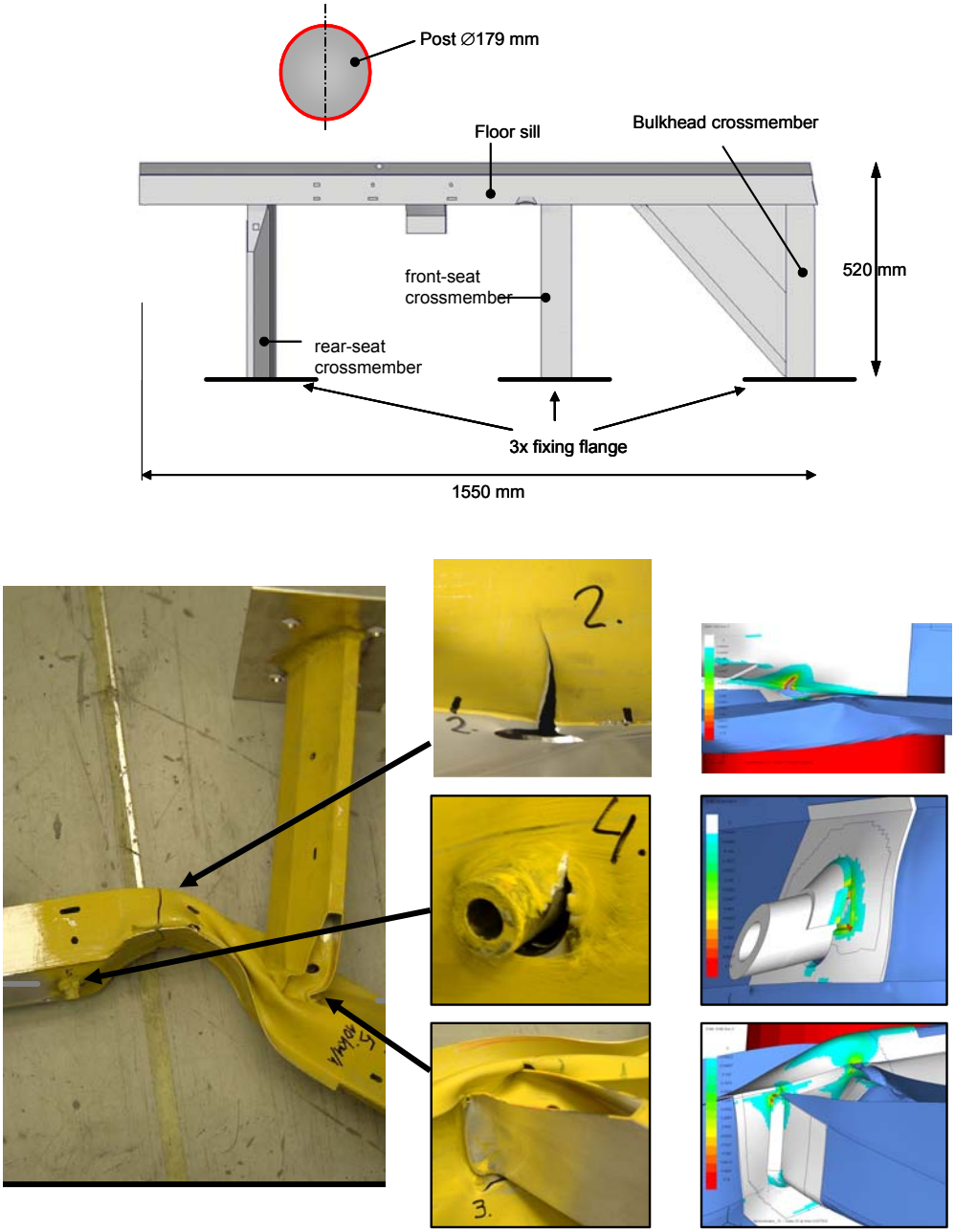

Fig 6: Experimental setup for space frame Aluminium structure and comparison of the observed test and simulation failure locations

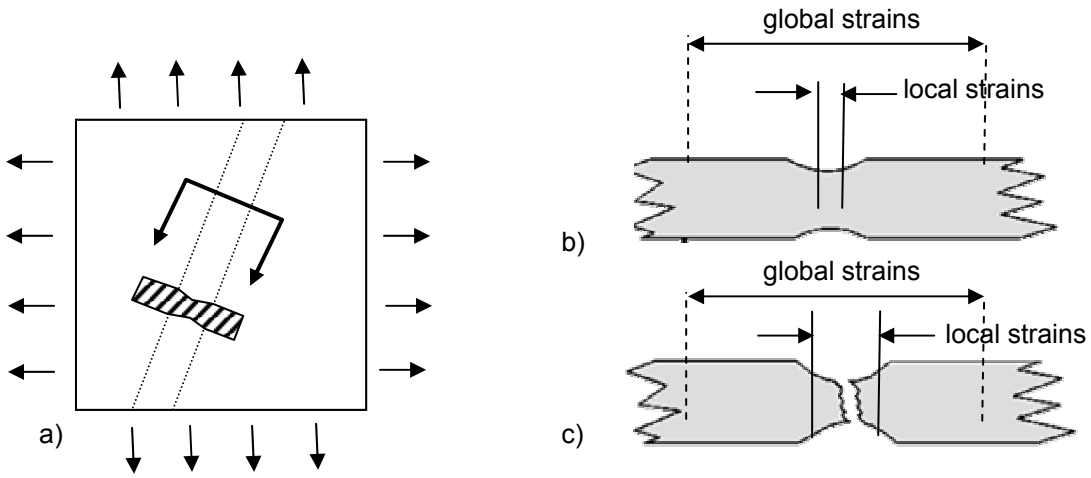

Fig 7: Local and global strains:

a) The Marciniak instability model

b) Onset of instability (local strains ≡ global strains)

c) Fracture (local strains >>global strains)

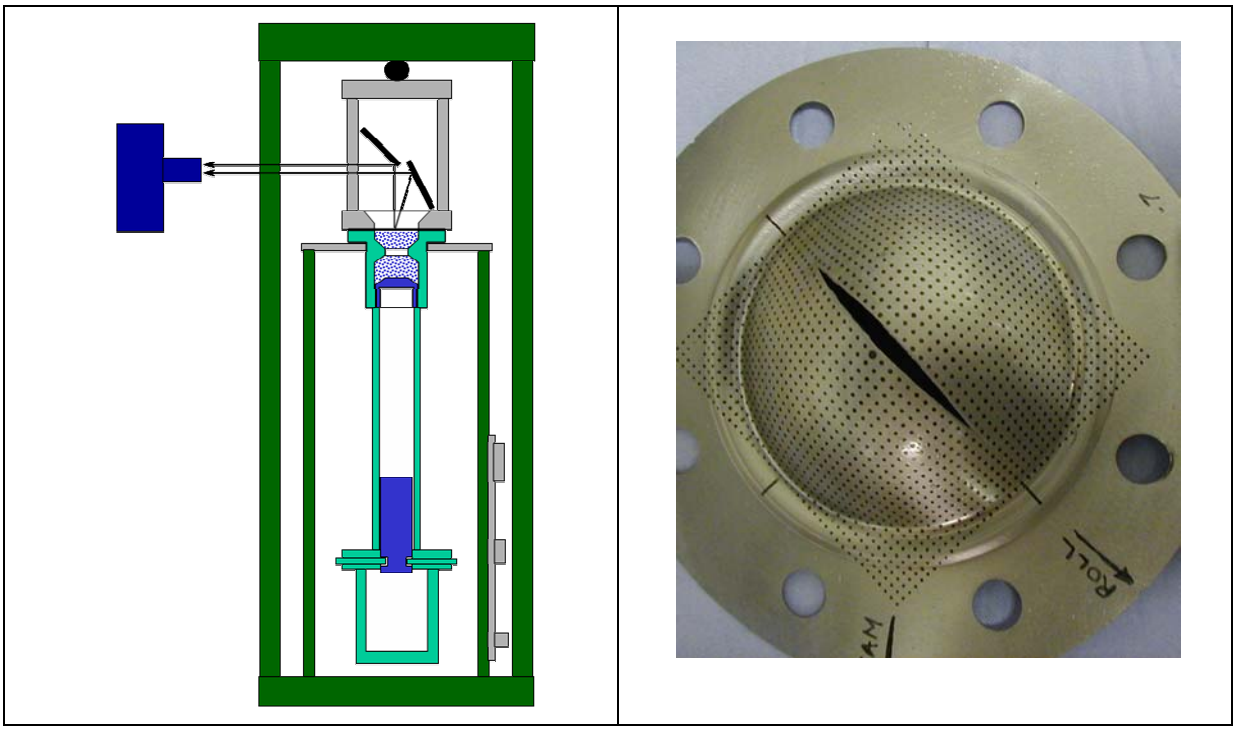

Fig 8: Rig for the dynamic bi-axial bulge test and a failed specimen after loading

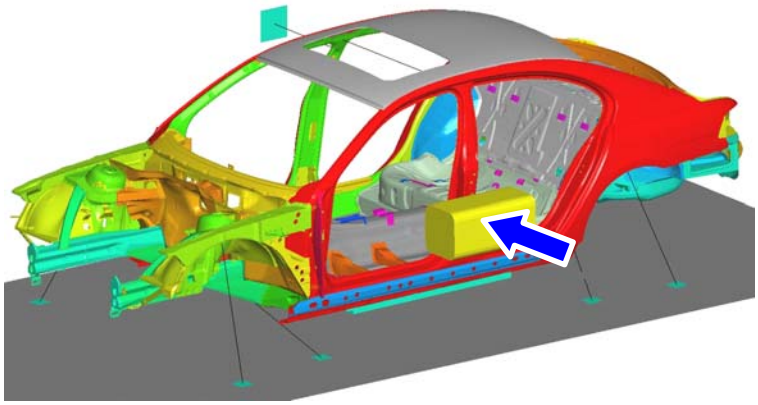

a) The body in white structure

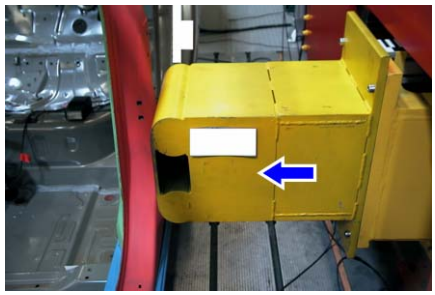

b) The loading setup

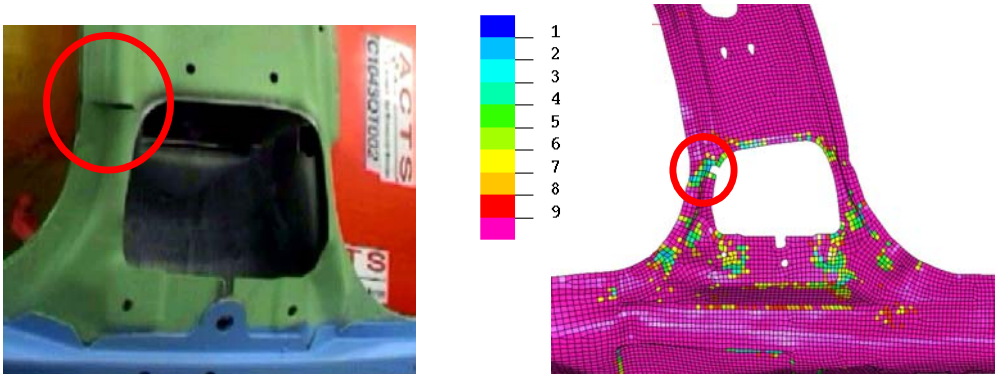

c) Test and simulation results showing critical location for failure

Fig 9: Side impact simulation and failure prediction using a macro- failure criteria

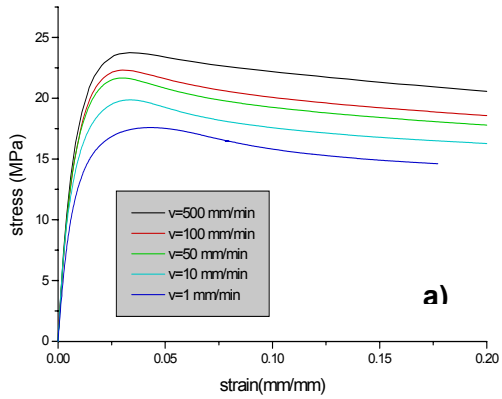

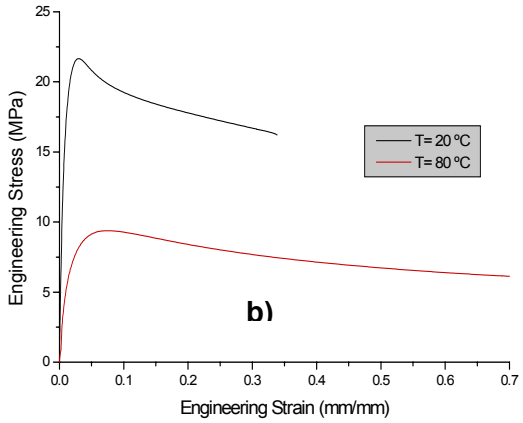

a) Strain rate dependence **b) Temperature dependence**

Fig 10: Typical stress versus strain curves for Polypropylene (PP)

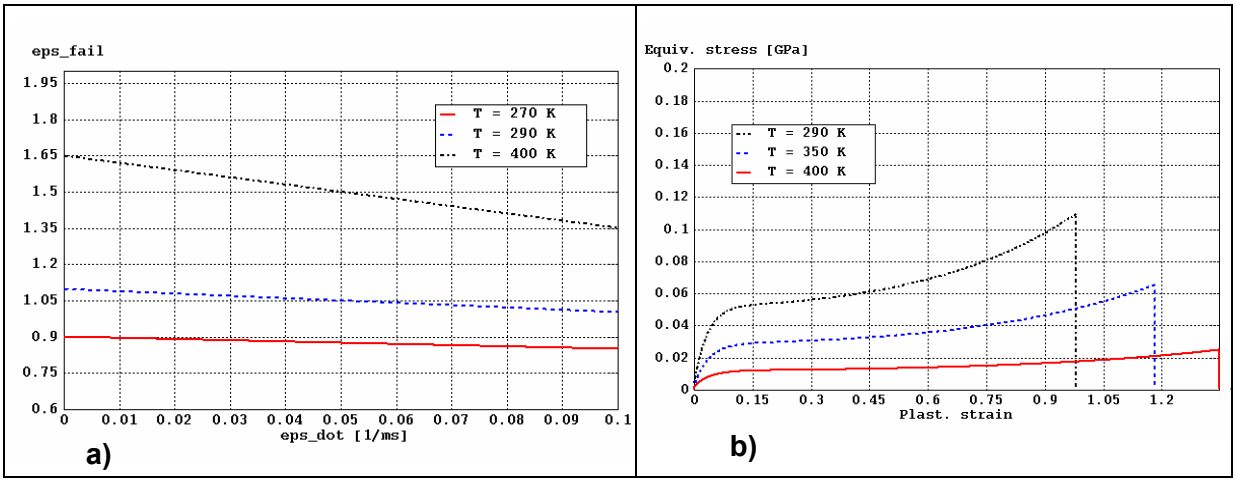

Fig 11: Failure and stress-strain curves:

a) Definition of failure b) Stress-strain curves with failure (strain rate =0.1sec^{-1})

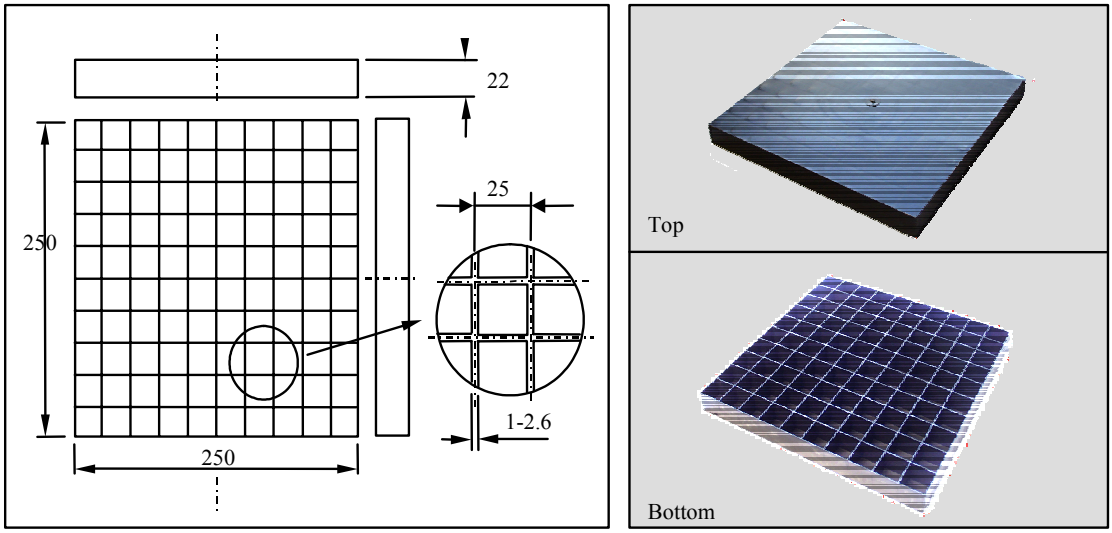

Fig 12: Geometry of the plastic honeycomb plate

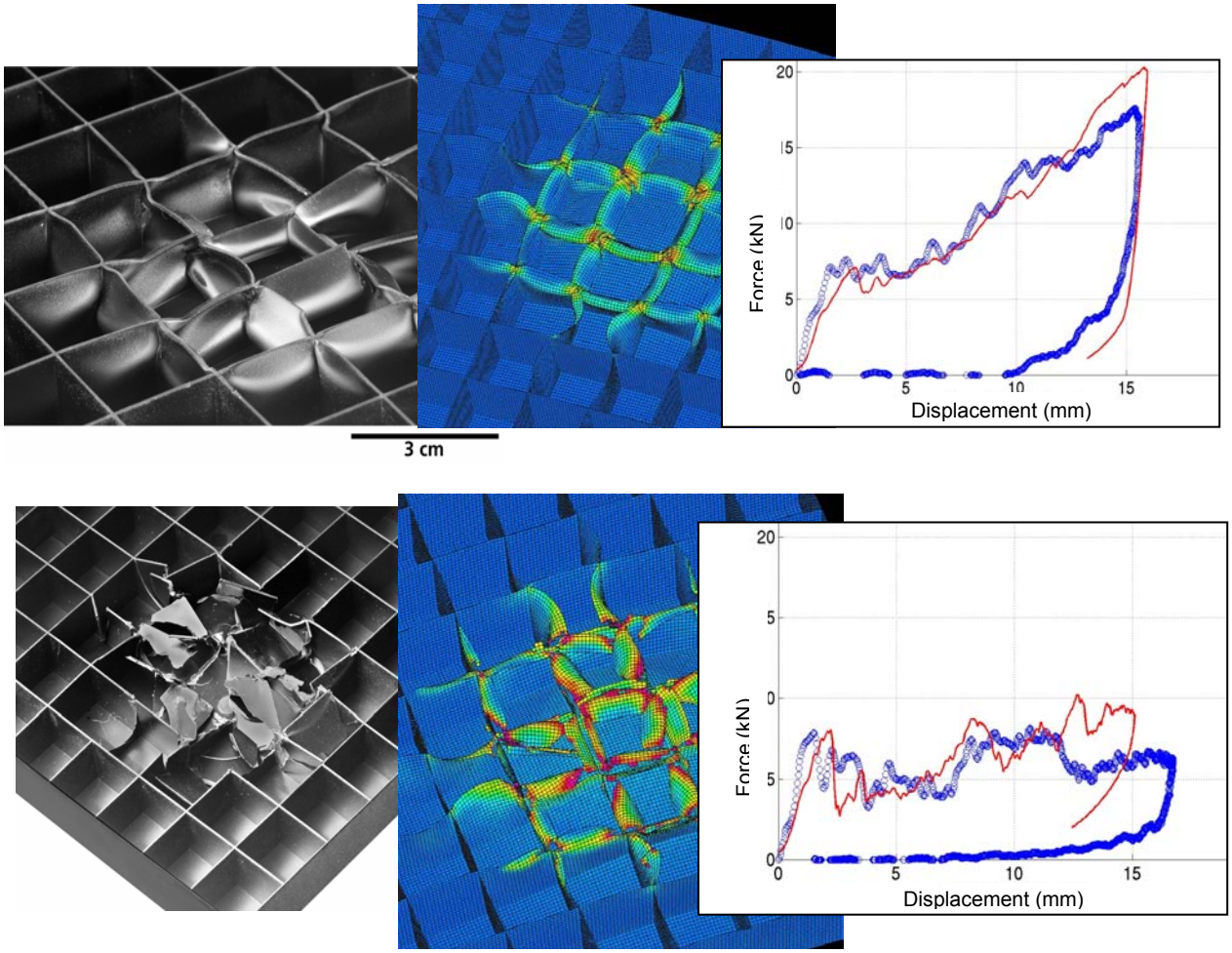

Fig 13: Comparison of experimental and simulation results for deformation and impact force on the honeycomb plastic panel: a) 85°C (above) b) 35°C (below)

		-15°C	20°C	85°C
k	**[MPa]**	66,725	55,249	34,497
w	**[-]**	63,661	73,982	104,693
h	**[-]**	1,264	1,308	1,349
m	**[-]**	0,0182	0,0299	0,0319

Table 2a: G'Sell Parameters for BAYBLEND for three temperatures

		-15°C	20°C	85°C
k	**[MPa]**	0,044	0,027	0,015
w	**[-]**	231	144	60
h	**[-]**	1,79	0,73	0,54
m	**[-]**	0,055	0,055	0,093

Table 2b: G'Sell Parameters for HIFAX for three temperatures

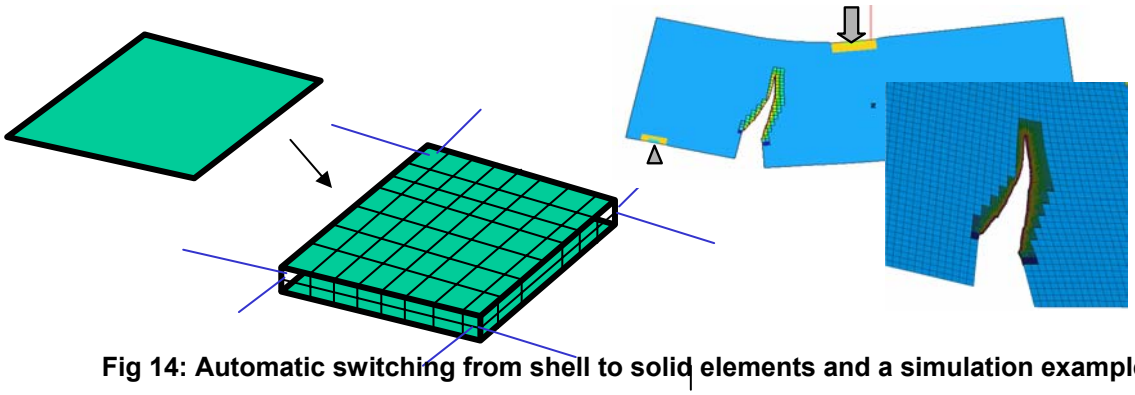

Fig 14: Automatic switching from shell to solid elements and a simulation example

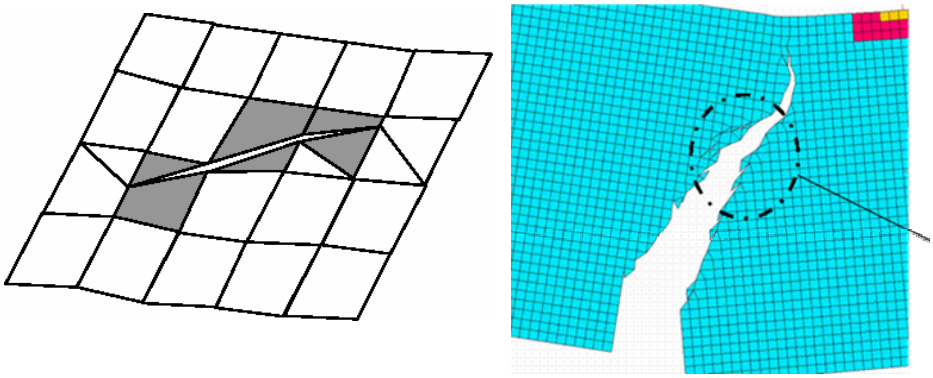

Figure 15: Principal idea of shell element splitting and an FE example